Segmentation, Separation and Pose Estimation of Prostate Brachytherapy Seeds in CT Images

Huu-Giao Nguyen, Céline Fouard, and Jocelyne Troccaz*, *Senior Member, IEEE*

Abstract*—*Goal: **In this paper, we address the development of an automatic approach for the computation of pose information (position + orientation) of prostate brachytherapy loose seeds from 3-D CT images.** ***Methods:*** **From an initial detection of a set of seed candidates in CT images using a threshold and connected component method, the orientation of each individual seed is estimated by using the principal components analysis method. The main originality of this approach is the ability to classify the detected objects based on *a priori* intensity and volume information and to separate groups of closely spaced seeds using three competing clustering methods: the standard and a modified k-means method and a Gaussian mixture model with an expectation-maximization algorithm. Experiments were carried out on a series of CT images of two phantoms and patients. The fourteen patients correspond to a total of 1063 implanted seeds. Detections are compared to manual segmentation and to related work in terms of detection performance and calculation time.** ***Results*:** **This automatic method has proved to be accurate and fast including the ability to separate groups of seeds in a reliable way and to determine the orientation of each seed.** ***Significance:*** **Such a method is mandatory to be able to compute precisely the real dose delivered to the patient postoperatively instead of assuming the alignment of seeds along the theoretical insertion direction of the brachytherapy needles.**

***Index Terms*—CT image, image segmentation, mixture model, prostate brachytherapy, radioactive seed, 3-D object location and pose estimation.**

I. Introduction

PROSTATE cancer is one of the leading cancers in men worldwide with 152 new cases and 23 deaths per 100 000 men reported worldwide per year from 2006–2010 (based on SEER Cancer Statistics Review) [1]. Low-risk prostate brachytherapy treatment that uses low dose rate radioactive seeds, has emerged as a common and highly effective method to manage localized prostate cancer. The typical implantation procedure is summarized as follows (see Fig. 1): Based on dose planning, lines of seeds (stranded or loose) are implanted through parallel needles. These needles are inserted into the prostate through the skin of the perineum using continuous transrectal ultrasound (US) guidance and following a preimplantation planning. Once accurate needle placement has been confirmed, the seeds are released through the needles. This process is continued until all seeds have been implanted. In practice, the number of seeds implanted in the prostate commonly ranges from 40 to 100. The goal of a successful operation is to position the seeds in order to get the proper dose coverage throughout the prostate while limiting the risk for the neighboring organs.

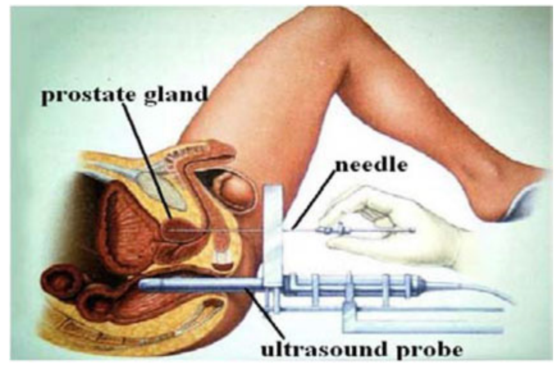

Fig. 1. Prostate brachytherapy implant technique (source http://www.prostatespecialist.co.uk).

In theory, the seeds are aligned in the needle insertion direction. Fig. 2(a) illustrates such a planning scheme. However, in practice the seed implantation depends on many biomechanical factors as well as human experience. The seeds may lose their intended position in spite of any special care or effort used when placing the needles and delivering the seeds [see Fig. 2(b)]. The examination of images [computed tomography (CT), X-ray, US or MRI] often shows that the seeds are not aligned in the implantation direction especially when using loose seeds. In this later case, the implantation may also result in groups of closely spaced seeds. In this paper, we name such a group a *union-seed*. Fig. 3 shows an example of seed organization in a single CT slice (including one union-seed). In addition, some seeds can migrate out of the prostate as reported by Gao *et al*. [2].

For treatment quality assessment, fluoroscopic images can be acquired immediately after seed implantation. But generally CT data are also acquired one month after the intervention and a CT-based postimplant dosimetry is performed. The delay is such that any inflammatory modification of the prostate has disappeared and the dose computed from the seed positions can be considered as the real delivered dose. Most existing commercial treatment planning software (e.g., VariSeed, Interplant or PSID Brachytherapy software [4]) work under the assumption that all seeds are aligned with the CT axis [as shown in Fig. 2(c)]. However, the American Association of Physicists in Medicine recommends to determine the 3-D dose distribution of brachytherapy seeds based on real seed positions and

Manuscript received July 10, 2014; revised October 24, 2014 and January 16, 2015; accepted February 19, 2015. Date of publication March 6, 2015; date of current version July 15, 2015. This work was supported by grants from INSERM (Dorgipro Project PC201114) and from ANR (CAMI Labex ANR-11-LABX-0004). *Asterisk indicates corresponding author.*

*J. Troccaz is with UJF-Grenoble 1/CNRS/TIMC-IMAG Laboratory, Grenoble F-38041 France (e-mail: jocelyne.troccaz@imag.fr).

H.-G. Nguyen and C. Fouard are with UJF-Grenoble1/CNRS/TIMC-IMAG Laboratory.

Color versions of one or more of the figures in this paper are available online at http://ieeexplore.ieee.org.

Digital Object Identifier 10.1109/TBME.2015.2409304

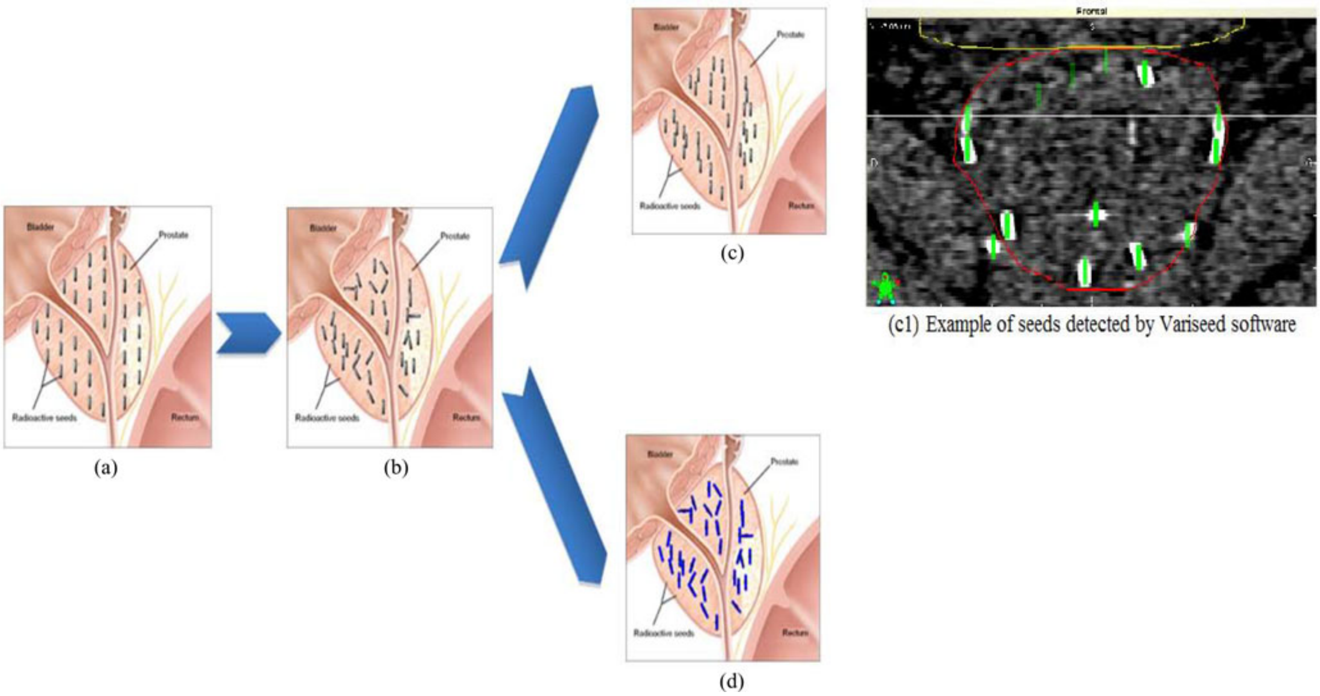

Fig. 2. Seed distribution in prostate brachytherapy: (a) seeds aligned with the insertion direction as defined in the planning (from http://cancer.uc.edu/cancerinfo/TypesOfCancer/ProstateCancer/InterstitialBrachtherapy.aspx); (b) real distribution of seeds one month after the implantation; (c) and (c1) seed distribution as handled by existing commercial software; (d) seed distribution detected by the proposed method.

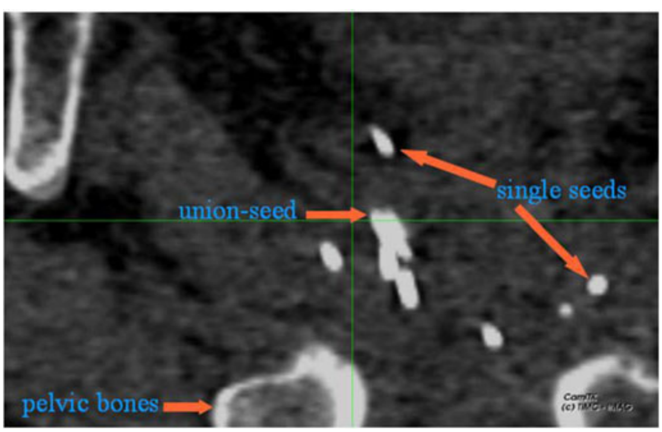

Fig. 3. Example of implanted seeds as visible in a single slice of a CT image.

orientations [3]. A related clinical question is: "*Does taking into account real seed orientation induce significant differences in dose distribution of brachytherapy treatment?*." The Dorgipro project we participate in aims to answer this question by comparing the distributed dose calculated using standard brachytherapy software (which assumes that the orientation is the planned orientation) to dose distribution obtained when considering the 3-D real seed orientation. This paper focuses on the imaging aspects of this research project. The medical physics aspects are described in a companion paper and will be briefly summarized in Section V of this paper.

This paper presents the image processing method used to extract the seed positions and orientations, i.e., five parameters (due to the cylindrical shape of the seeds). Our objective is thus to develop a fully automatic software that is able to detect seeds, separate groups of seeds—this stage is also referred to as declustering in the literature—and accurately determine the 5-D pose of seeds. In this study, we exploit the high intensity appearance of radioactive seeds in CT images for a solution based on threshold and connected component segmentation [5]; we also consider volume information for outlier removal and computation of the number of seeds in a union-seed. Three declustering methods are considered for union-seed separation: the k-means-based method [7] and a modified version of it and the Gaussian mixture model (GMM) with an expectation-maximization (EM) algorithm [8]. Finally, the principal components analysis (PCA) method [6] for orientation estimation is applied. Reference data coming from the manual segmentation of seeds are used to validate the proposed method.

This paper is organized as follows. We begin by examining the state-of-the-art in prostate brachytherapy seed detection in medical images in Section II. In Section III, we present the proposed solution for seed segmentation (see Section III-A), union-seed separation (see Section III-B) and orientation estimation (see Section III-C) of the prostate brachytherapy seeds in CT images. Experiments and evaluation are reported for datasets generated from phantoms and 14 anonymous patients in Section IV. We then discuss the main contributions and potential extensions of the proposed approach in Section V.

II. Related Work

The accurate localization and orientation estimation of brachytherapy seeds, including the ability to separate union-seeds, is a major challenge and active research field. Numerous

TABLE I
EXISTING BRACHYTHERAPY SEED DETECTION SYSTEMS AND THEIR INNOVATIONS

Author Ref	Year	Imaging Modality	Image Dimensionality	When?	Using Planning	Stranded \ Loose	Position Detection	Orientation Estimation	Declustering	Seed Types (3)	Tests(4)
D'Amico *et al.* [10]	2000	MRI	3D	IO(1)		N/G(2)	X			Id	C
Su *et al.* [11]	2004	X-ray	n2D(5)	IO or IPO		N/G	X		X	N/G	C+P
Wei *et al.* [12]	2006	US	3D	IO	X	L	X	X		D	P
Singh *et al.* [13]	2007	X-ray	n2D	N/G		N/G	X			N/G	C+P
Fallavollita *et al.* [14]	2010	CT	3D	IO		N/G	X			N/G	C+P
Kuo *et al.* [15]	2010	MRI	3D	N/G		N/G	X			D	P
Lee *et al.* [16]	2011	X-Ray	2D	IO		N/G	X			Pd	C
Moult *et al.* [17]	2012	X-Ray	2D	IO		N/G	X		X	Id	C+P
Moult *et al.* [18]	2012	X-Ray	2D	IO		N/G	X		X	N/G	C
Defghan *et al.* [19]	2012	X-Ray	n2D	IO or IPO	X	N/G	X			Pd	C+P
Kuo *et al.* [20]	2012	X-Ray	2D	IO		N/G	X		X	Pd	C+P
Chng *et al.* [21]	2012	CT	3D	IPO or PO		S	X	X		Id	P
San Silippo *et al.* [22]	2013	X-Ray	n2D	IO or IPO		N/G	X		X	Id	C
Hu *et al.* [23]	2013	Cone beam CT	3D	IO	X	N/G	X		X	Id/Pd	C
San Filippo *et al.* [24]	2014	X-Ray	n2D	IO or IPO	X	L	X		X	Id+Pd	C
Kuo *et al.* [25]	2014	X-Ray	n2D	IO or IPO	X	N/G	X		X	Pd	C+P
Proposed method	2014	CT	3D	PO		L	X	X	X	Id	C+P

1) IO: intraoperative; IPO: immediate postoperative; PO: or postoperative. 2) N/G: Information is not given. 3) D: dummy seed; Pd : Palladium 103; Id: Iodine125. 4) P: phantom; C: clinical data. 5) n2D: multiple 2-D images.

studies [9]–[25] have been published based on different prostate image modalities, including magnetic resonance (MR), US, X-ray and CT images. As previously mentioned, determining seed positions is useful at different stages of the clinical protocol: During the implantation US and/or X-ray images are necessary for simply monitoring seed deposition or for intraoperative dynamic dosimetry [12], [22]–[24] and iterative correction in case of inaccurate delivery; X-ray images are also used immediately after the implantation for recording purpose; finally, CT data are most often used after one month for dose evaluation. MRI can also be used postoperatively alone or in combination with CT. These modalities have different advantages and drawbacks: US is a nonradiating modality as compared to X-ray but seeds are more difficult to detect in US due to resolution, noise and reflection artifacts. Whilst MRI is nonradiating, CT is more often used for dosimetric planning and evaluation since it provides useful information about tissue radiological density. X-ray-based modalities enhance seed visibility while US or MRI improve the visibility of the prostate and other soft tissue. Clusters of seeds visible in the images may arise either from an inaccurate delivery of loose seeds or from an occlusion of stranded seeds in X-ray projections. These specificities have given birth to a very large collection of methods. Whilst our approach is for the detection of loose seeds in CT postoperative images we give a brief overview of some of the developed methods, with a summary in Table I. They are classified according to different properties:

1) the three required abilities: segmentation, 3-D orientation estimation and declustering,
2) the imaging modalities and dimensionality,
3) when they are used (intraoperative IO, immediate postoperative IPO or postoperative PO),
4) whether or not they use the planning information,
5) the type of seeds (stranded or loose—Palladium or Iodine), and
6) how they were evaluated (phantom study, clinical study).

Note that Table I does not contain data about commercial software as there is very little information available, they effectively work as "black boxes." To the best of our knowledge no commerical software provides capabilities similar to the one described in this paper.

Recent advances in X-ray images have been reported for position detection and declustering of prostate seeds: for example, the partition division on multiple projections of C-arm fluoroscopic images [11], [16], the region-based segmentation implicit active contour model [17], [18], the geometric analysis from the graph matching problem [13] or the mathematical morphology analysis [20]. However, these methods may require a sophisticated object-matching algorithm and/or calibration to deal with the substantial distortion of seeds in fluoroscopic images; moreover the orientation of seeds was not considered.

The other modalities, US and MRI, have also received a lot of attention in the last decade. For example, the appropriate location estimation of seeds in a target volume of real-time MR imaging [10] or in IRON images (inversion-recovery with on-resonant water suppression) using the Laplacian of a Gaussian technique for blob detection [15] was considered. Wei *et al.* [12] segmented the seeds from the subtraction map between the background and postimplant US images and then applied a PCA method for orientation detection. Again, these methods do not manage union-seeds and the orientation of the seeds and their detection results are limited by the poor visualization of seeds in US and MR images.

Other approaches are based on the coregistration of different image modalities. For instance, a series of methods [14], [19], [22], [24], [25] propose a volume-to-volume and point-to-volume registration scheme of US images with the implants reconstructed from fluoroscopy. Recently, Hu *et al.* [23] considered the prior knowledge of the US-to-CT transformation via registration and the planning seed position to define an atlas of

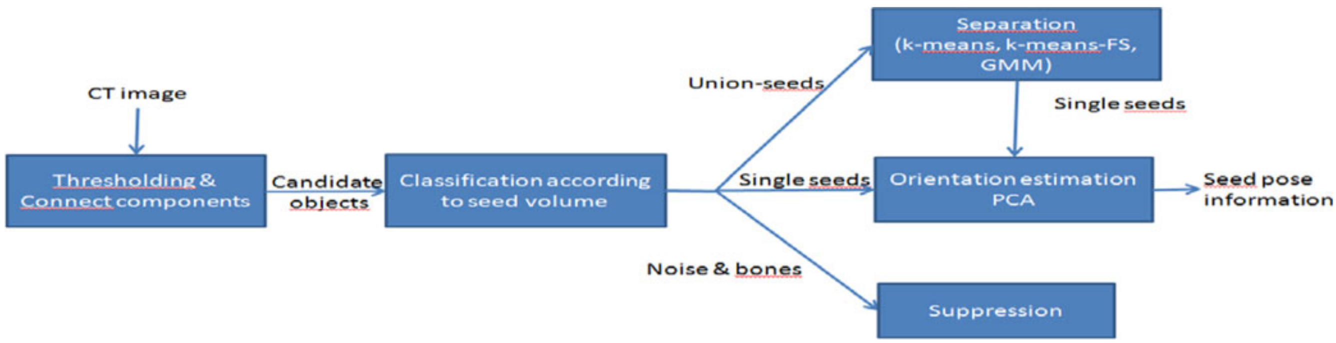

Fig. 4. Main steps of our proposed approach.

regions of interest for seed detection. Union-seed separation was considered, however there was no explicit mention concerning the management of seed orientations in these approaches.

Many papers consider stranded seeds whose real orientation is generally quite similar to the planned orientation, making it possible to search for lines of seeds close to the planned orientation. For instance, Chng *et al.* [21] estimated the seed orientations from the tangent vector to the curve of a seed strand identified in postimplant CT images at each seed position.

Because loose seeds enable the clinician to sculpt the dose to the precise treatment constraints, our objective was to develop a method allowing the use of these loose seeds. Thus, this study addresses the development of an automatic image processing solution for the segmentation, localization and orientation estimation of prostate seeds. Fig. 2(d) shows an illustration of the expected result of the proposed method for the detection of seed poses in the prostate from the analysis of CT scanner images.

III. Methods

Fig. 4 shows a sketch of the proposed approach. The different steps of this method are further detailed in the following sections, including:

1) 3-D object segmentation and classification for the detection of a set of seeds (single and union-seeds) in Section A.
2) Union-seeds separation in Section B.
3) 3-D orientation estimation in Section C.

A. Seed Segmentation Using the Connected Object Labeling Method and Seed Classification Using the k-Means Method

This section details the detection of a set of seed candidates and their classification into three groups (outliers, single seeds and union-seeds) (see Fig. 5). Brachytherapy seeds are small metallic cylinders (typically about 1-mm diameter for 5-mm length) and appear as high intensity objects. They may produce local artifacts obscuring neighboring tissues. Numerous methods have been developed to segment such small objects in a gray level image including some region-based methods such as watershed transformation [26], [27] and level sets [28], [29]. However, these methods require user input by positioning initial seeds or shapes. We choose to use *a priori* knowledge about Hounsfield values in CT images [30], as well as volume information about the seeds in order to limit user interaction.

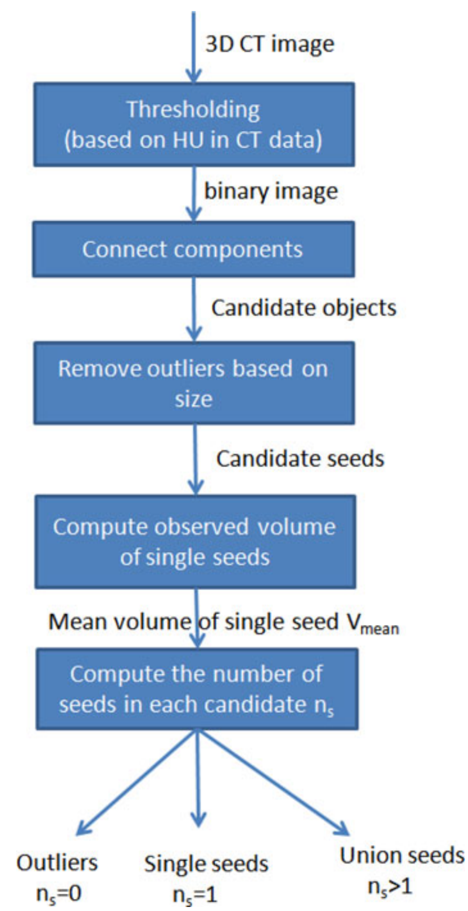

Fig. 5. Detail of seed segmentation and classification step.

For instance, the voxel intensities of each type of material in the CT images processed in this study are [min, 400] for phantom material and for patient soft tissues, [0, 1350] for bones and [500, max] for seeds. Here, a threshold-based segmentation method, namely *connected component labeling* [5] with only an intensity threshold parameter t, is considered to exploit this information for the detection of individual objects in the images. We first threshold the original volume with the threshold parameter t, then each connected component (using 26-connectivity) is assigned a label i and ordered by its size. The location of each component is determined as its center of mass c_i.

It is evident that the choice of the intensity threshold t is a key issue. It can be heuristically set based on the image

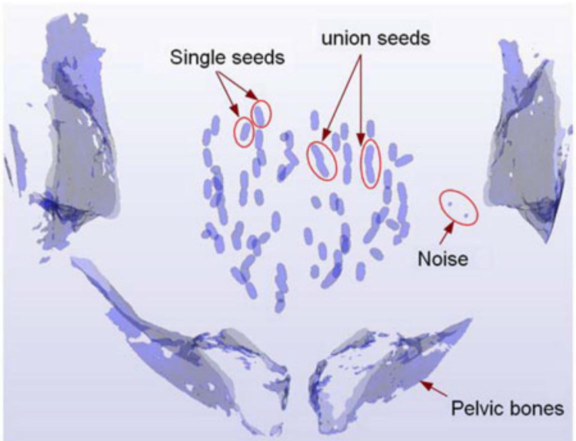

Fig. 6. Example of connected component detection in a 3-D CT image with 190 objects obtained using an intensity threshold of 700.

characteristics and on the physical characteristics of the X-ray absorption of the seeds (see Section IV). Moreover, the proposed method minimizes its influence on the results. Indeed, as the choice of the threshold affects the volume of the obtained connected component, no absolute volume is used, but the relative volumes of the components are compared to each other. Fig. 6 shows an example of connected components detected in the CT image of a patient, for a given threshold. The detected objects in CT images of patients are divided into four types, including: single seeds, union-seeds, bones and noise.

Comparing the volumes of the detected components to the real volume of the seeds allows the first coarse classification of the objects detected in the images. Let us denote by $V_{\rm real} = \pi r^2 l$ the real volume of a radioactive seed, where *r* is the radius and *l* the length of seed. The next step aims at suppressing large and small objects as compared to $V_{\rm real}$. In practice, the pelvic bones are very large components (with volumes more than 100 times larger than the real volume $V_{\rm real}$). Conversely, noise is composed of tiny components (with volumes smaller than a third of $V_{\rm real}$). The other components are kept as candidate seeds with two types: single seeds and union-seeds. In practice up to four or five seeds can be included in a union-seed; however, generally only two seeds are grouped. Determining the number of seeds in a union-seed requires an estimation of the seed volume observed in the CT exam; this volume clearly depends on the threshold *t*.

Without loss of generality, we can assume that single seeds outnumber union-seeds in the remaining candidates (connected components). Indeed, even if union-seeds often appear in loose seed insertions, despite care taken by the clinician, they remain exceptions and most seeds are placed with a reasonable distance between them. We thus investigated the use of an unsupervised partitioning method, *k-means clustering* [7] to separate the candidate seeds into k groups based on volume analysis. As mentioned, most detected components correspond to the cluster of single seeds; we therefore decided to add two other clusters for smaller (if any) and larger objects (in particular including unions seeds); thus, we set $k = 3$. Fig. 7 shows an example of k-means clustering on the volume of seed candidates detected in the CT image of a real patient with 85 radioactive seeds implanted.

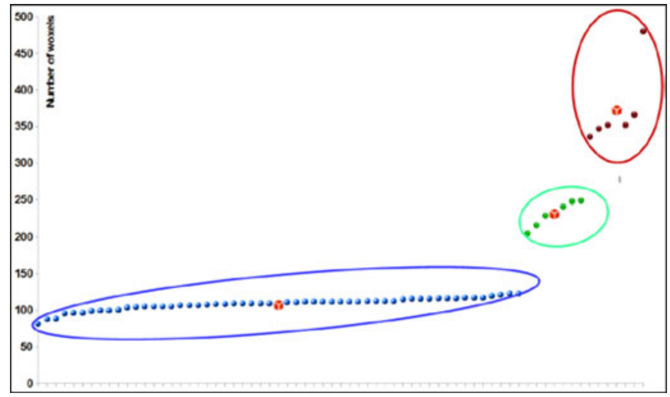

Fig. 7. Example of the result of the k-means method applied to the volume histogram of connected components detected in CT13 image (see Section IV). 66 components are assigned to three clusters (represented by blue, green, red circle points). The red square points correspond to the mean volume of each cluster. Here, the largest cluster with 54 members is considered as the cluster of single seeds.

The detail of the general *k-means* method is as follows: We first randomly select k points as the initial cluster centroids. Then, each candidate is assigned to the closest centroid of k clusters based on volume information. We iterate this process until stability is reached. The *k-means* algorithm shows its computational simplicity in many classification applications. However, the resulting clusters strongly depend on the selection of the initial centroids. To improve the classification of seeds, the three initial centroids of clusters are defined as: the minimum, mean and maximum volume of the detected candidate components. At the end of the process, the largest cluster is selected as the set of single seeds with average volume $V_{\rm mean}$ computed from the cluster. This value of $V_{\rm mean}$ is considered as the observed volume of a seed in the image given by the threshold *t*. This is a very important element to make the method more robust with respect to the choice of *t*. The final classification of the components is based on the comparison of their volume to $V_{\rm mean}$. The number of seeds corresponding to each candidate is calculated (rounded to the nearest integer value) as follows:

$$n_s = V_{\rm component}/V_{\rm mean} \tag{1}$$

where $V_{\rm component}$ is the volume of the candidate component. At the end of this process, components are classified as follows:

1) $\mathrm{n_s} = 0$: The component is considered as an outlier and removed;
2) $\mathrm{n_s} = 1$: The component is considered as a single seed;
3) $\mathrm{n_s} > 1$: The component is considered as a union-seed composed of n_s seeds.

Declustering the union-seeds will be necessary before pose determination; it will be presented in the next section.

B. Union-Seed Separation

Considering the set of voxels of each union-seed detected by the connected component labeling and the number of seeds n_s grouped in this union-seed [see (1)], this second step aims at separating union-seeds using three unsupervised learning procedures: a *k-means,* a modified version named *k-means-FS* and

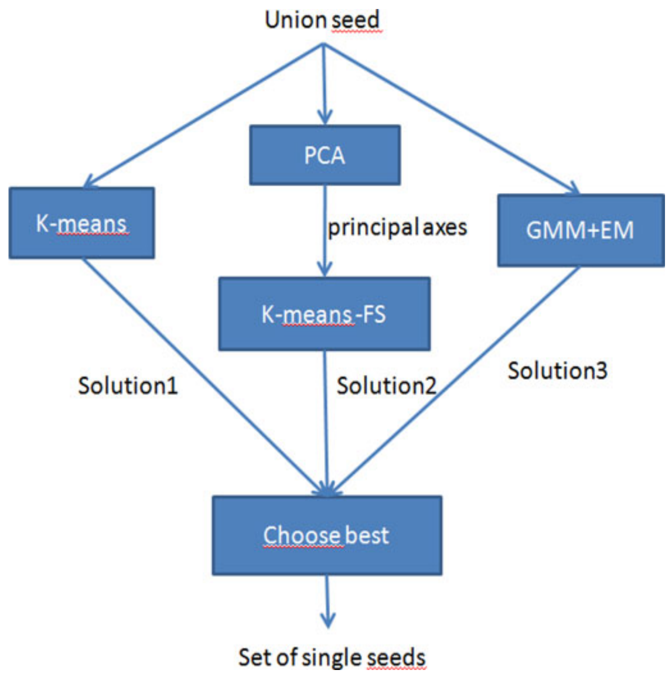

Fig. 8. Detail of union-seed separation step.

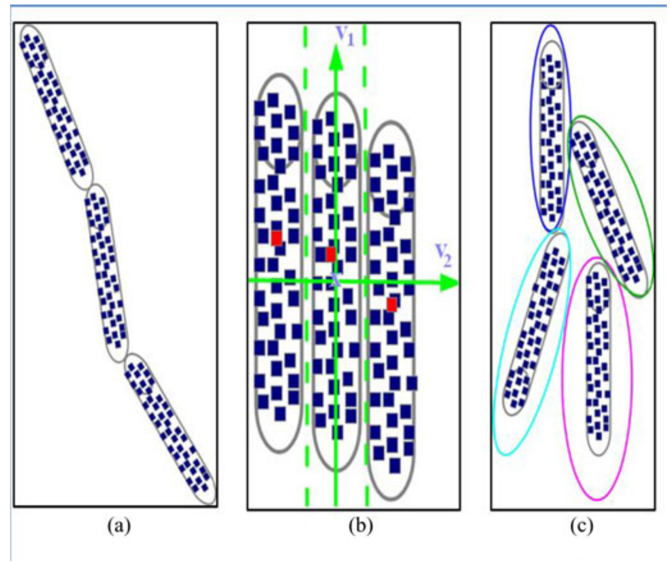

Fig. 9. Seed separation. (a) Case where the standard k-means algorithm works well and two more difficult cases: (b) k-means-for-seeds method with the choice of the initial centroid to improve the clustering performance of k-means, where the red point are the centroids of the k partitions, x is the centroid of the union-seed, the dotted-lines are used to determine the k-1 parallel planes w.r.t. the distance $d = \lambda_2/k$. (c) separation result obtained using the GMM with the EM algorithm.

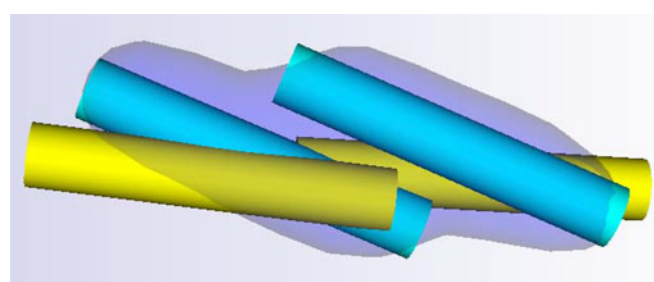

Fig. 10. Example of the separation result for a parallel union-seed (detected voxels visualized in blue) with two methods: classical k-means (yellow cylinders) and k-means-FS (cyan cylinders). In this case, the best solution is achieved using k-means-FS.

a *GMM* method. Fig. 8 shows the detail of this step. These three methods enable handling cases that none alone can treat properly. The *k-means* clustering method is again used for the voxel locations of each union-seed to separate it. Here, k is given for each union-seed by the computed number n_s [in (1)] and the method groups voxels based on their proximity in terms of position. However, the resulting seed clusters of *k-means* also depend on the selection of the initial centroids and on the size and shape differences between the regions shared in the clusters. In practice, the separation of a straight union-seed [see Fig. 9(a)] is easily achieved by this classical *k-mean* method. In contrast, the inaccuracies of this method occur when trying to separate groups of parallel seeds [see Fig. 9(b)] or groups of four or five seeds that are closely spaced [see Fig. 9(c)]. Hence, we introduce two other methods to improve the separation of union-seeds. The first method consists in choosing the initial cluster of the *k-means* algorithm by exploiting the orientation information given by the PCA method (denoted *k-means-for-seeds*); it is intended to more robustly separate groups of parallel seeds. The second method makes use of the *GMM* with the EM algorithm [8] for better processing of complex groups of seeds.

1) Introducing the k-Means-for-Seeds Method: We define the *k-means-for-seeds (k-means-FS)* method as follows: First, two main directions $\{v_1, v_2\}$ of the union-seeds are estimated using the PCA method (see Section III-C). Then, $(n_s - 1)$ parallel planes are defined by the main direction v_1 of the union-seeds and the distance $d = \lambda_2/n_s$ between them [see Fig. 9(b)], where λ_2 is the second eigenvalue of the covariance matrix C of the union-seed. These parallel planes divide the union-seed space into n_s partitions. Finally, we apply the *k-means clustering* algorithm with the initial cluster centers that are the centroids of these n_s partitions. In practice, this method presents its strength in solving the problem of parallel seeds. Fig. 10 shows an example of the application of the basic *k-means* and *k-means-FS* for a parallel union-seed separation. Note that the seeds displayed in Figs. 10 and 11 are the results with their pose information estimated using the PCA method.

2) Using the GMM and the EM Algorithm: In some cases, the k-means-FS method does not give optimal results; thus, we also consider a GMM in order to improve the clustering of complicated union-seeds containing four or five seeds [see Fig. 9(c)]. Each cluster of the GMM is generated by initially choosing a cluster and then drawing from that cluster's Gaussian distribution (with means μ_i and covariance C_i). The probability given in a mixture of k Gaussians is given by

$$p(x) = \sum_{i=1}^{k} w_i N(x|\mu_i, C_i) \tag{2}$$

where w_i is the prior probability (weight) of the *i*th Gaussian, $\sum_{i=1}^{k} w_i = 1$ and $0 \leq w_i \leq 1$. The parameters $\theta = \{w_i, \mu_i, C_i\}$ of the *i*th Gaussian component are learned by the maximum

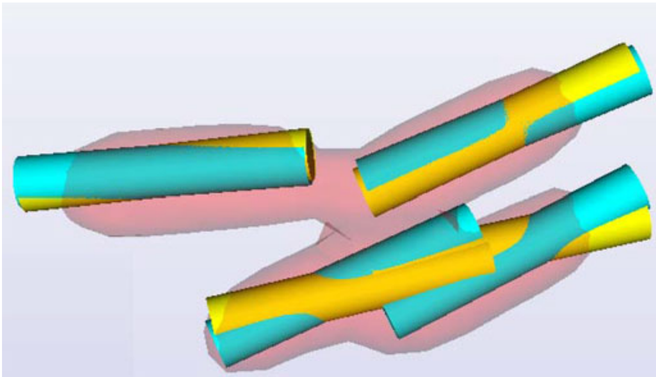

Fig. 11. Separation result of a union-seed with four closely spaced seeds using two methods: k-mean-FS (yellow cylinders) and GMM with the EM algorithm (cyan cylinders). The original detected union-seed voxels are visualized in red. In this case, the best solution is given by the GMM and EM algorithm.

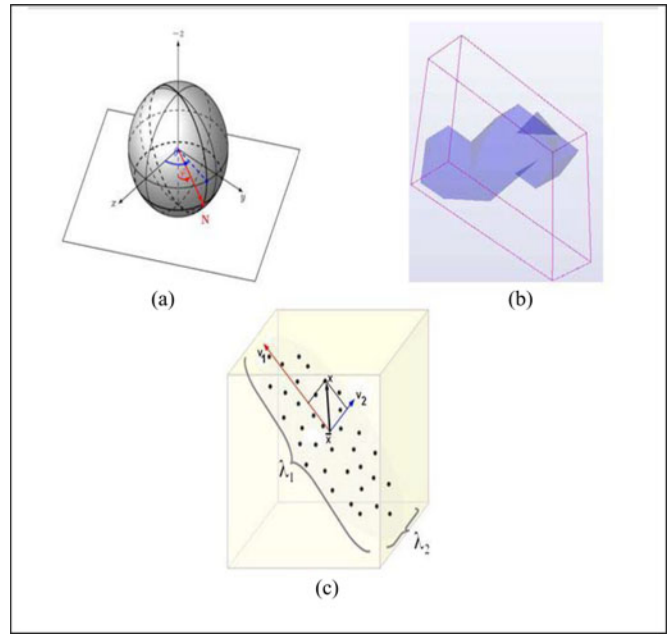

Fig. 12. Different approaches for 3-D orientation estimation of a 3-D cloud of points: (a) Hough transform (image is taken from [33]). (b) minimal bounding box. (c) principal components analysis.

likelihood estimation. The log likelihood function takes the form

$$\begin{aligned}\ln p\left(X|w,\mu,C\right) &= \sum\nolimits_{j=1}^{N} \ln\left(\sum\nolimits_{i=1}^{k} wi\ N\left(x_j|\mu_i,C_i\right)\right)\\ &= L(\theta|X).\end{aligned} \tag{3}$$

In this maximum likelihood problem, we try to find a set of parameters θ that maximizes L(θ|X) using the standard EM algorithm [8]. This algorithm works as follows: We initialize an estimation of a set of Gaussian parameters θ. Here, the means μ_i are obtained by the k-means algorithm, the covariance matrices C_i are calculated from the distance to the nearest cluster of k-means and all Gaussian weights w_i are equally likely. At each iteration of the EM algorithm, we compute the expected values of the unknown data given the observed data and the current model parameters in the expectation (E) step. The maximization (M) step involves optimizing and updating the parameters to be those with maximum likelihood. It can be shown that the log-likelihood was improved at each such iteration. This process is stopped if a local maximum has been reached or some stopping criterion is met, e.g., the default number of iterations. Fig. 11 shows an example of the seed separation improvement using the GMM method compared to the k-mean-based method when applied to a complex union-seed with four closely spaced seeds.

3) Selection of the Best Separation Method: In order to achieve robustness, for each union-seed, we run each of the three methods: the classical *k-mean* method with different random selections of the initial centroid clusters, the *k-means-for-seeds* method and the *GMM* with *EM* algorithm. For each of the methods, the cylindrical shapes corresponding to the model of the seeds are positioned as computed. For each solution, the sum of the number of voxels common between these cylindrical shapes and the union-seed detected in the image is calculated. The solution with the largest common volume is selected as the best one.

In our clinical experiments reported in Table IV of Section IV-C, 116 union-seeds in 14 patients were achieved. Among them the best solution was found for 30 cases (25,9%) using the k-means-for-seeds method, 18 cases (15,5%) using the GMM method and 68 other cases (58,6%) using the classical k-means method.

The obtained single seeds are then processed in order to compute their orientation as described in Section III-C.

C. Orientation Estimation Using the PCA Method

In this third step, we aim to estimate the orientation of each 3-D object detected by the connected component labeling or union-seeds declustering. Numerous approaches have been proposed to estimate the 3-D object orientation in point clouds. Among the most popular, the 3-D Hough transform [31]–[33] focuses on the definition of the 3-D Hough space of each point [see Fig. 12(a)]. The computational complexity is a major drawback of the Hough transform approximated by O(s^{p-1}n), where *n* is the number of points, *p* is the number of parameters and *s* is the number of samples along one Hough dimension. Another category of 3-D orientation estimation is based on finding minimal enclosing boxes [34], [35]. Approximate minimum-volume bounding box methods [see Fig. 12(b)] were shown to be particularly efficient with a complexity of O(n+1/$\varepsilon^{4.5}$) compared to the Hough transform approaches, where ε is the approximation parameter. Such minimum bounding box models are however not well-suited to our problem because they require a heuristic parameter ε for grid search of the bounding box. This parameter ε has no physical meaning related to the CT image acquisition.

In this study, we focused on a solution for 3-D orientation estimation that would improve both aspects, by investigating the PCA method [6]. The PCA method is the simplest and most robust mathematical procedure for compressing and extracting the description of a set of correlated observations by rejecting low variance features. Considering p-dimensional feature vectors (in our case, 3-D), the PCA method is the projection of this data onto q principal components. The first principal component v_1 is the feature space along which projections have the largest eigenvalue λ_1 of the covariance matrix C of the point cloud. This is chosen as the orientation of the object [see Fig. 12(c)]. The second principal component v_2 is the direction which maximizes the variance among all directions orthogonal to the first one. The second direction v_2 is exploited for the separation step of union-seeds.

IV. Experiments and Evaluation

A. Experimental Setup

As mentioned in Section II, various methods have been developed for different types of seeds. In Europe, the most frequently used isotope for permanent prostate seed implantation is Iodine-125 (see the edition 2011 of Radiotherapy in Practice—Brachytherapy [36]). That is why we focused on such type of seeds. The validation of the proposed method, described in this section, was done using CT images of brachytherapy seeds implanted into: 1) two specially created phantoms and 2) data from 14 real patients provided by the Grenoble University Hospital.

1) Radioactive Iodine-125 Seed: The clinical team of the Grenoble University Hospital uses BEBIG IsoSeed I-125 seeds. A seed is made of a cylindrical-shaped ceramic material, saturated with radioactive Iodine-125 compound and a gold marker located in the center, all enclosed by a laser-sealed titanium tube. The outer physical dimensions of the seed are $l = 4.5 \pm 0.2$ mm length and $r = 0.4 \pm 0.02$ mm external radius. The Iodine-125 isotope emits photons at a maximum energy of 35 keV and has a half-life of 59.46 days. This information is provided by the manufacturer [37]. Note that, the Iodine-125 was taken off for the case of phantom to avoid the risk of radioactive contamination.

2) CT Images: The 3-D CT images were obtained using a GE Lightspeed RT16 scanner with the default X-ray tube parameters: 120 kVp, 380–440 mA·s. The slice thickness was 0.625 mm with 16 frames/s for each slice. The image reconstruction matrices were 512 × 512 archived in DICOM 3.0 format with 16-bit gray-level intensities. These acquisition parameters were experimentally determined by the medical physicists using phantoms so that the seeds could be seen on three to five slices [39].

3) Evaluation: In this paper, the evaluation of the proposed approach is given in three terms: location and orientation detection performance and calculation time. A fully automatic software based on the proposed solution was built on the open-source framework CamiTK [38] (using C++ with VTK and ITK libraries). This software also provides some postprocessing tools to verify seed by seed in case of errors or inaccuracy. The user can modify the seed position to better fit the image data; this manually edited seed location is the reference information to which the automatic detection is compared.

For this, we used the Euclidean distance between their centroids c and c_{ref} and the dot product of their orientation vectors v and v_{ref} [see (4)].

$$\Delta d = \sqrt{\sum_{i=1}^{3} (c_i - c_{iref})^2}, \Delta\theta = \text{acos}\left(\frac{v.v_{ref}}{||v||\,||v_{ref}\,||}\right) \quad (4)$$

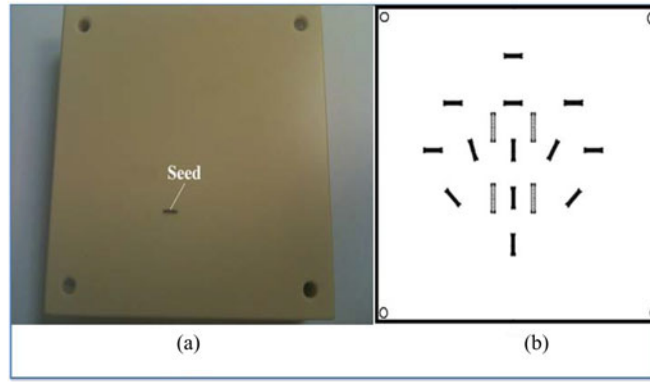

Fig. 13. Water equivalent phantoms: (a) single seed in a slab phantom (cf., Section IV-B1); (b) seeds located on the surface of the central slab of the other phantom (cf., Section IV-B2).

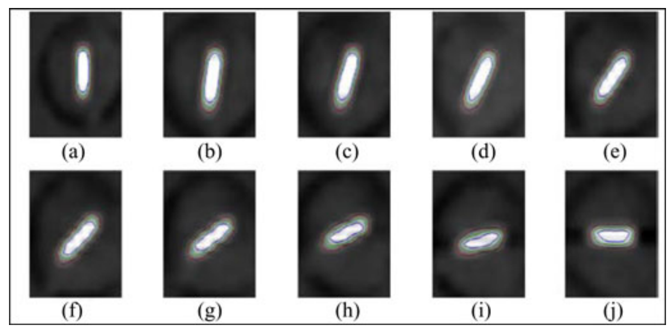

Fig. 14. Detection of a seed with different orientations. The overlaid curves are the detected contours for different intensity thresholds.

where $||v_i||$ is the magnitude of the vector v_i, the unit of distance Δd is expressed in mm, and $\Delta\theta$ is in degrees. Here, the time evaluation is on a computer of 3.4-GHz Intel Core i7-2600 CPU.

B. Phantoms

The medical physicists of the clinical team created two phantoms (see Fig. 13) wherein the seeds were precisely positioned with different orientations on the surface of the slab. Both phantoms had the same physical dimensions of $9 \times 9 \times 0.5$ cm^3. The reference position of the seeds in the phantom based on manual detection was also provided for each case.

1) Single Seed in a Slab Phantom: The first phantom [cf., Fig. 13(a)] that we considered had a single seed located in certain "predefined" orientations to evaluate the pose detection of the proposed method. The 3-D image size of this phantom is 512 × 512 × 41 and the voxel size is 0.199 × 0.199 × 0.625 mm^3. We created 11 orientation cases for this phantom. Fig. 14 illustrates the different orientations of the seeds positioned in this phantom.

Table II shows the values of the reference orientations and the comparison between the results of the proposed method and the reference with respect to orientation $\Delta\theta$ and distance Δd when using an intensity threshold of $t = 1500$. With this value, the greatest $\Delta\theta$ orientation error of 1.69° is observed for the case (i) (for about 70°) and the other cases are equal to or smaller than 0.83°. The best detection was obtained with the

TABLE II
DETAILS OF THE ORIENTATION DIFFERENCES $\Delta\theta$ AND DISTANCES ΔD BETWEEN THE DETECTED POSE OF THE SEEDS AND THEIR REFERENCE VALUE FOR $t = 1500$ (IN DEGREES AND MILLIMETERS)

	0°	10°	20°	30°	40°	45°	50°	60°	70°	80°	90°
Ref.	0.12	9.65	20.72	30.1	39.8	45.2	49.8	60.8	69.1	79.4	90.2
$\Delta\theta^{\circ}$	**0.20**	0.83	0.54	0.76	0.54	0.63	0.65	0.71	**1.69**	0.70	0.51
Δd^{mm}	**0.02**	0.08	0.14	0.18	0.12	0.10	0.14	0.20	**0.26**	0.16	0.06

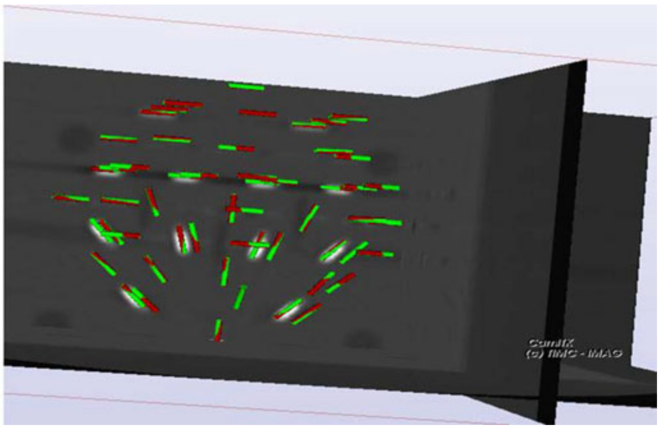

Fig. 15. 3-D CT scanner image of the second phantom and the distribution of the 73 seeds: Theoretical positions of seeds are painted in green and detected seeds are in red.

reference orientation close to 0° (seed perpendicular to the CT acquisition plane) where $\Delta\theta = 0.2°$ and $\Delta d = 0.02$ mm. Additionally, to investigate the dependence of the proposed method to the choice of *t*, we also ran this experiment with ten choices of *t* in an interval of [800, 1700]. The mean value and the standard deviation of the orientation error are $\Delta\theta = 0.96° \pm 0.4$. The mean value and standard deviation of the distance error are $\Delta d = 0.08 \pm 0.04$ mm.

2) Multiple Seeds in a Multislab Phantom: We also report a second experiment about the detection of 73 seeds implanted in a more complex phantom composed of nine slabs (Plastic water-LR, Medi-Test, Saclay, France). The placements of the seeds look more similar to what could be a real implantation for a patient. Nine same size slabs are pressed together by four screws. Holes were drilled into the slabs to place the radioactive seeds in different orientations. Fig. 13(b) shows the design of the central slab of the phantom. The 3-D image size of this phantom is 512 × 512 × 73 and the voxel size is 0.217 × 0.217 × 0.625 mm^3. In this experiment, we have tested the proposed method with ten choices of *t* in the interval of [800, 1700]. Fig. 15 shows the distribution of the 73 seeds detected in a CT image when using the intensity threshold $t = 1500$.

Compared to the reference data, the mean and standard deviation of the orientation error are $\Delta\theta = 1.32° \pm 0.9$; the mean and standard deviation of the position error is $\Delta d = 0.13 \pm 0.07$ mm for ten choices of the intensity threshold *t*. Some seeds are perfectly located ($\Delta\theta = 0°$, $\Delta d = 0$mm), e.g., the seeds positioned vertically in the central slab when using an intensity threshold of $t = 1500$. In contrast, the most inaccurate

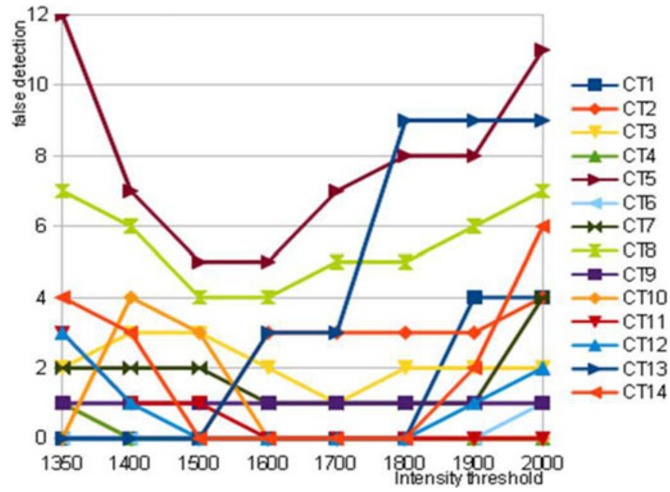

Fig. 16. Number of FDs obtained for the different choices of the intensity threshold t for the 14 cases.

detections were found for the oblique seeds, where $\Delta\theta = 1.8°$ and $\Delta d = 0.65$ mm.

C. Patient Experiment

We report 14 cases of radioactive seed detection on real patient images. The CT scanner images were taken one month after the implantation procedure in the Grenoble University Hospital. Data were anonymized before export and processing. Table IV details the information of the scanner images and the number of seeds implanted in the planning of the brachytherapy treatment. It should be reminded that, some seeds may migrate, therefore the number of detected seeds may be different even if perfectly successful.

In this experiment, we ran the proposed method with different values of the intensity threshold *t* for all 14 patient cases. Again, the choice of the intensity threshold *t* was based on the HU values of each material in the CT images: In these data, soft tissues were in the range [min, 400], bones were in [0, 1350] and seeds were in [500, max]. We considered the intensity threshold in the interval of [1350, 2000] with a step of 100 (beginning with 1400).

Seed detection errors, which we will call "false detections" (FD), can be classified into three categories as follows:

1) FD1: the undetected seeds because of their migration out of the imaged region or because of the limitations of the method (false negative).
2) FD2: the noisy objects detected in image such as calcifications that can be recognized as potential seeds if their intensity and volume are compatible with the seeds or union-seeds characteristics (false positive).
3) FD3: correspond to the errors due to the incorrect separation of union seeds; that may be due to a wrong estimated number of seeds.

The sum of all types of FD, when using the proposed method with different values of the intensity threshold *t* in the range [1350, 2000], is plotted in Fig. 16. Here, the best results were obtained with the thresholds $t = 1500$ or 1600 where the sum of

TABLE III
CUMULATED NUMBER OF FDs FOR THE 14 CASES AS A FUNCTION OF THRESHOLD VALUE t

t	1350	1400	1500	1600	1700	1800	1900	2000
ΣFD **/total**	3.4%	2.6%	**1.8%**	**1.8%**	2%	2.7%	3.5%	4.8%

Here, the total number of implanted seeds is 1063 for 14 cases.

FD are minimum for all 14 patient cases. When a low threshold t (e.g., $t = 1350$) is chosen, FD2 increases with extra noise. In contrast, the number of wrongly separated seeds (FD3) is bigger when a high threshold t (e.g., $t = 1900$) is used; this is because of the loss of shape information of the seeds. The total number of FD, summed from the 14 cases, for each choice of threshold t is given in Table III.

From this experimental result, we suggest choosing the intensity threshold in Hounsfield Units in [1500, 1700], for which the radioactive seeds can be most successfully separated from the other material.

Table IV details the results obtained for the 14 prostate cases using the proposed method with an intensity threshold of $t = 1500$. Compared to the reference data, the maximum (respectively minimum) orientation error $\Delta\theta$ is 3.180° $\pm$ 0.9 (resp. 0.680° $\pm$ 0.2) and the maximum (resp. minimum) distance error Δd is 0.50 $\pm$ 0.16 mm (resp. 0.15 $\pm$ 0.09 mm). The number of FD is also reported in detail for each case. Compared to the number of implanted seeds, eight seeds in total could not be found (FD1) in CT3, CT5, CT7, CT8 and CT9 images. Some existing objects of FD2 type were also detected in CT3 (cf., Fig. 17), CT5, CT7, CT10 and CT11. Considering FD3 FDs (wrong union-seed separation), two groups of four real implanted seeds were detected as union-seed of five seeds; this occurs in CT3 and CT5 images.

Fig. 18 also shows the detail of each type of FD for a single patient (CT14) and for different values of the threshold t. The mean calculation time of the proposed method was 9.7 s over 126 runs for 14 patient cases with different intensity thresholds t. It is therefore a very fast solution when compared to the half day that was required for the careful manual segmentation of the reference data or compared to the average 30 min for conventional postprocessing of images treated by our clinical team after detection of seeds with their commercial system. Fig. 19 shows some examples of the seeds detected in patients.

V. DISCUSSION

In this study, an efficient and fast approach for the pose estimation of brachytherapy seeds in CT images has been presented. The key methods used in this study may be summarized as follows:

1) Classification of detected objects based on *a priori* intensity and volume information.
2) Estimation of 3-D objects based on the extraction of principal components.
3) Separation of groups of seeds using k-means, a modified k-means clustering method and GMM method with an EM algorithm.
4) Individual seed orientation estimation using the PCA method.

The results herein were quickly obtained with only small differences compared to the reference data for both phantoms and patients. For example, the proposed method achieves the orientation error $\Delta\theta = 0.96^\circ \pm 0.4$, the distance error $\Delta d = 0.08 \pm 0.04$ mm and the calculation time 0.67 s $\pm$ 0.3 for a phantom in Section IV-B1. These evaluation values can be compared to $\Delta\theta = 2^\circ$, $\Delta d = 0.3$ mm and calculation time 9 s of a previous related work for CT images (Chng's method [21]). This comparison in terms of detection performance and calculation time pointed out the relevance of our contributions. However, these comparisons must be interpreted carefully since the phantoms and computer systems were different.

In clinical practice, the role of the human operator can be limited to a verification task and modifications for misdetections if any. In fact, the migrated seeds (FD type: FD1) always lead to a significant uncertainty in the postimplant dosimetry calculation. The proposed method described in this paper works without the prior knowledge about the number of implanted seeds. Therefore, finding less seeds than expected by the planning should warn the operator about possible migration or misdetections. On the other hand, the false positive detections (FD2) are often due to calcifications very frequent in the prostate gland of men with benign prostatic hypertrophy and prostate cancer. The distinction between calcifications and brachytherapy seeds may be still a challenging task even for a very skilled clinician. Thus, the verification by the clinician in this case is always necessary but may not be sufficient.

The advantage of the clustering approaches (k-means or GMM) used in this study for the separation of union-seeds is their small computational complexity compared to other approaches such as RANSAC [40] or Hough transform [33]. However, there was still a few FDs due to inappropriate seed separation (here, FD3): less than 0.19% (see Table IV). Therefore, a manual correction step may also be necessary. Some approaches based on the morphology analysis or 3-D template matching could be considered in the future to improve the performance of this separation task. Overall of 1063 seeds implanted in 14 patient cases in Table IV, the false positive (FD2 + FD3) percentage of our approach is 1.03%. This value is lower compared to the state-of-the-art methods reported in the Table II of the publication of San Filippo *et al.* [24], where [17] was 2.2%, [22], [24] were 1.7%. These results open the door to accurate dose calculation and procedure quality assessment. As already mentioned in the introduction, a dosimetry study has been launched in parallel in our institution on a series of patients including the 14 patients of this paper [39]. Its aim is to evaluate the impact of accurate pose evaluation onto dose distribution for prostate brachytherapy treatment. It will be published separately but a few elements may be summarized here. Compared to the ideal axis of insertion, the seeds angular error are in average for the 1063 seeds of the 14 patients 0.81° $\pm$ 27.7 and 1.06° $\pm$ 21.1 in spherical coordinates. As concerns the Dose Volume Histograms no significant difference could be demonstrated between dose evaluation using or not orientation information but our number of patients was quite small. In a very recently published paper

TABLE IV
DETAILED RESULTS FOR 14 CT SCANNER IMAGES OF PATIENTS

Case	Image size	Voxel size	Max. intensity	Nb of seeds implanted	FD			Seeds detected						$\Delta\theta°$	Δd (mm)	Time(s)
					FD1	FD2	FD3	Single	Union-seeds				Total			
									2	3	4	5				
CT1	$512 \times 512 \times 91$	$0.266 \times 0.266 \times 0.625$	6766	77	0	0	0	39	13	4	0	0	77	1.53 ± 0.5	0.29 ± 0.14	8.6
CT2	$512 \times 512 \times 91$	$0.283 \times 0.283 \times 0.625$	7749	71	0	0	0	41	6	2	3	0	71	2.51 ± 0.5	0.41 ± 0.18	7.2
CT3	$512 \times 512 \times 91$	$0.355 \times 0.355 \times 0.625$	4625	79	1	1	1	69	3	0	0	1	80	1.91 ± 0.7	0.30 ± 0.12	11.7
CT4	$512 \times 512 \times 111$	$0.244 \times 0.244 \times 0.625$	6122	72	0	0	0	64	4	0	0	0	72	0.97 ± 0.3	0.17 ± 0.08	10.1
CT5	$512 \times 512 \times 76$	$0.322 \times 0.322 \times 0.625$	5620	89	1	**3**	**1**	53	15	1	0	1	91	2.79 ± 1.1	**0.50 ± 0.16**	**13.7**
CT6	$512 \times 512 \times 66$	$0.250 \times 0.250 \times 0.625$	5905	77	0	0	0	55	11	0	0	0	77	1.24 ± 0.5	0.23 ± 0.10	8.9
CT7	$512 \times 512 \times 111$	$0.381 \times 0.381 \times 0.625$	6321	76	1	1	0	61	6	0	0	0	73	1.75 ± 0.8	0.12 ± 0.07	9.3
CT8	$512 \times 512 \times 101$	$0.344 \times 0.344 \times 0.625$	5373	80	4	0	0	66	5	0	0	0	76	1.01 ± 0.6	0.21 ± 0.09	10.4
CT9	$512 \times 512 \times 129$	$0.189 \times 0.189 \times 0.625$	6451	81	1	0	0	66	4	2	0	0	80	1.17 ± 0.4	0.17 ± 0.06	11.8
CT10	$512 \times 512 \times 111$	$0.434 \times 0.434 \times 0.625$	5185	73	0	3	0	66	5	0	0	0	76	0.73 ± 0.4	0.29 ± 0.14	11.7
CT11	$512 \times 512 \times 81$	$0.293 \times 0.293 \times 0.625$	4060	64	0	1	0	57	4	0	0	0	65	***0.68 ± 0.2***	***0.15 ± 0.09***	8.5
CT12	$512 \times 512 \times 91$	$0.291 \times 0.291 \times 0.625$	5689	72	0	0	0	55	7	1	0	0	72	1.45 ± 0.6	0.27 ± 0.10	9.0
CT13	$512 \times 512 \times 91$	$0.297 \times 0.297 \times 0.625$	6281	85	0	0	0	54	6	5	1	0	85	2.15 ± 0.7	0.28 ± 0.11	9.1
CT14	$512 \times 512 \times 101$	$0.348 \times 0.348 \times 0.625$	5462	67	0	0	0	37	9	3	1	0	67	**3.18 ± 0.9**	0.46 ± 0.15	***6.9***
					8	**9**	**2**									
		Overall		**1063**	**0.75%**	**0.84%**	**0.19%**									

Intensity threshold is $t = 1500$. The minimum intensity value (in HU) over the 14 cases is –3024. The three types of FDs are mentioned. The detected seeds are classified as: single, group of two, three, four or five seeds. The FD percentage is in the last line.

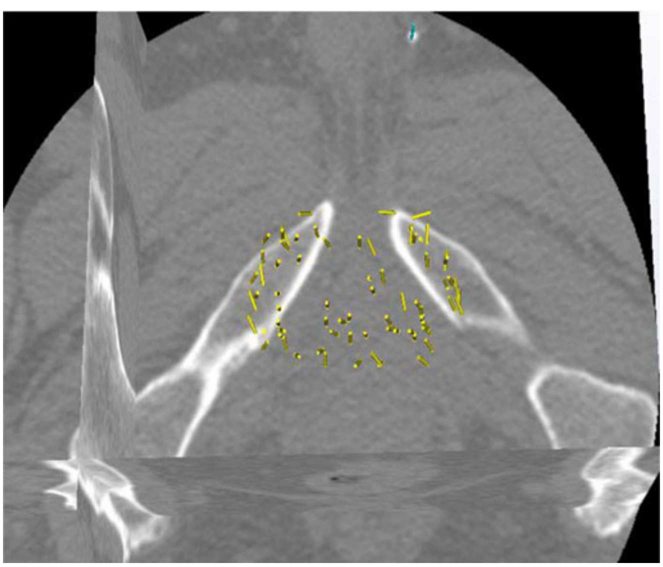

Fig. 17. Example of FD2 FD in CT3 with $t = 1500$ (cyan cylinder at the top of the image).[1]

[41] concerning a study using five fluoroscopic images and a CT of 287 patients, the authors demonstrate small but significant dose difference evaluated on organs at risks. In our much more limited study we also exhibited significant local dose differences that could have a clinical impact. A more extensive clinical study is necessary to draw useful conclusions. In the context of this study which aim was to evaluate a new method, man–machine interaction has been restrained to what was strictly necessary. It is clear that the routine use of the approach would require special care for assisting the operator in the verification task, in particular we envision to orient his/her screening toward suspicious detections. Work remains to be done for scoring the detection.

[1]In this example a smaller ROI would have allowed to avoid such a FD; however, we kept it because the visualization in this figure was easier than when FDs are in the middle of the other seeds.

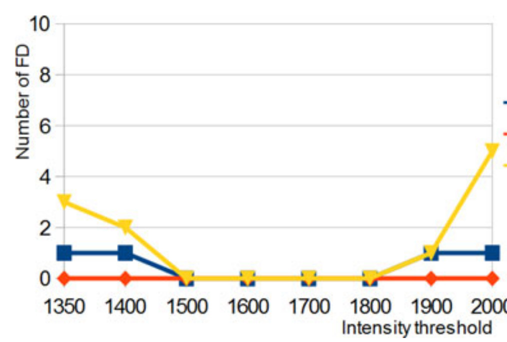

Fig. 18. Number of FD for different values of t for a patient example (CT14 case).

In future work, the potential of an automatic choice of an optimal intensity threshold will be further explored from the analysis of quantitative and geometric information of FDs. Robust solutions of seed localization for different prostate image modalities such as US or image registration for improved evaluation with respect to the anatomy of patient are also among the key issues that should be addressed.

VI. CONCLUSION

This paper has presented an automatic, accurate, robust and fast approach for the automatic localization of brachytherapy loose Iodine-125 seeds in CT postoperative images. It was evaluated on phantom and patient data. The key originalities of this study lie in the ability to separate groups of seeds and

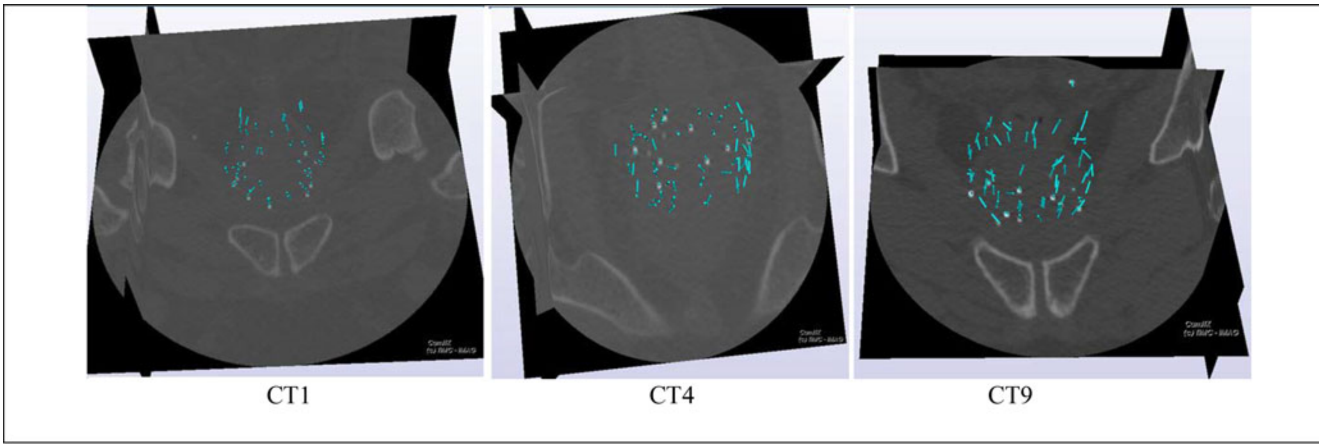

Fig. 19. Examples of seed detections for three patients.

to determine their orientation for improved evaluation of dose distribution to the patient. Based on intensity information and observed volume of the detected objects the method was able to accurate determine the 5-D pose of seeds with very few FDs. Further work both concerns technical aspects and a larger clinical evaluation.

Acknowledgment

The authors would like to thank F. Meneu, J.-Y. Giraud, C. Verry and M. Bolla from the Radiotherapy Department, Grenoble University Hospital, for providing their expertise and the clinical images used in this study. The authors would also like to thank C. Hughes and N. Hungr for critically editing the paper.

References

[1] N. Howlader *et al.*, "SEER cancer statistics review, 1975–2010," *National Cancer Inst.*, Bethesda, MD, USA, 2013.
[2] M. Gao *et al.*, "Effects of seed migration on post-implant dosimetry of prostate brachytherapy," *Med. Phys.*, vol. 34, pp. 471–481, 2007.
[3] M. Rivard *et al.*, "Update of aapm task group no. 43 report: A revised aapm protocol for brachytherapy dose calculations," *Med. Phys.*, vol. 31, no. 3, pp. 633–674, 2004.
[4] (2014). [Online]. Available: http://www.seedos.co.uk/dose_planning_equipment. htm
[5] L. Shapiro and G. C. Stockman, *Computer Vision*. Englewood Cliffs, NJ, USA: Prentice Halls, 2002, pp. 69–73.
[6] I. T. Jolliffe, *Principal Component Analysis*. New York, NY, USA: Springer, 2002.
[7] J. Han *et al.*, *Data Mining: Concepts and Techniques*. San Mateo, CA, USA: Morgan Kaufmann, 2011.
[8] A. Dempster, N. M. Laird, and D. B. Rubin, "Maximum likelihood from incomplete data via the em algorithm," *J. Royal Statist. Soc. B*, vol. 39, no. 1, pp. 1–38, 1977.
[9] J. Corbett *et al.*, "The effect of seed orientation deviations on the quality of 125i prostate implants," *Med. Phys.*, vol. 46, pp. 2785–2800, 2001.
[10] A. V. D'Amico *et al.*, "An image-guidance system for dynamic dosimetry in prostate brachytherapy using ultrasound and fluoroscopy," *J. Radiation Oncol. Biol. Phys.*, vol. 14, pp. 367–370, 2000.
[11] Y. Su *et al.*, "Prostate brachytherapy seed localization by analysis of multiple projections: Identifying and addressing the seed overlap problem," *Med. Phys.*, vol. 31, pp. 1277–1287, 2004.
[12] Z. Wei *et al.*, "Automated localization of implanted seeds in 3d trus images used for prostate brachytherapy," *Med. Phys.*, vol. 33, no. 7, pp. 2404–2417, 2006.
[13] V. Singh *et al.*, "Brachytherapy seed localization using geometric and linear programming techniques," *IEEE Trans. Med. Imag.*, vol. 26, no. 9, pp. 1291–1304, Sep. 2007.
[14] P. Fallavollita *et al.*, "Registration between ultrasound and fluoroscopy or CT in prostate brachytherapy," *Med. Phys.*, vol. 37, no. 6, pp. 2749–2760, 2010.
[15] N. Kuo *et al.*, "Mri-based prostate brachytherapy seed localization," in *Proc. IEEE Int. Symp. Biomed. Imag.*, 2010, pp. 1397–1400.
[16] J. Lee *et al.*, "Intraoperative 3D reconstruction of prostate brachytherapy implants with automatic pose correction," *Phys. Med. Biol.*, vol. 56, no. 15, pp. 5011–5027, 2011.
[17] E. Moult *et al.*, "Segmentation of iodine brachytherapy implants in fluoroscopy," *Int. J. Comput. Assisted Radiol. Surgery*, vol. 7, pp. 871–879, 2012.
[18] E. Moult *et al.*, "Implicit active contours for automatic brachytherapy seed segmentation in fluoroscopy," *Proc. SPIE*, vol. 8316, pp. 831611–831611, 2012.
[19] E. Dehghan *et al.*, "Ultrasound–fluoroscopy registration for prostate brachytherapy dosimetry," *Med. Image Anal.*, vol. 16, no. 7, pp. 1347–1358, 2012.
[20] N. Kuo *et al.*, "Automatic segmentation of radiographic fiducial and seeds from X-ray images in prostate brachytherapy," *Med. Eng. Phys.*, vol. 34, no. 1, pp. 64–77, 2012.
[21] N. Chng *et al.*, "Prostate brachytherapy postimplant dosimetry: Seed orientation and the impact of dosimetric anisotropy in stranded implants," *Med. Phys.*, vol. 39, pp. 721–731, 2012.
[22] C. A. di San Filippo *et al.*, "Declustering n-connected components for segmentation of iodine implants in C-arm fluoroscopy images," in *Proc. Inf. Process. Comput. Assisted Interventions*, 2013, pp. 101–110.
[23] Y. Hu *et al.*, "Fast radioactive seed localization in intraoperative cone beam CT for low-dose-rate prostate brachytherapy," *Proc. SPIE*, vol. 8671, pp. 867108-1–867108-8, 2013.
[24] C.A. di San Filippo *et al.*, "Intraoperative segmentation of iodine and palladium radioactive sources in C-arm images," *Int. J. Comput. Assisted Radiol. Surgery*, vol. 9, pp. 1–8, 2014.
[25] N. Kuo *et al.*, "An image-guidance system for dynamic dosimetry in prostate brachytherapy using ultrasound and fluoroscopy," *Med. Phys.*, vol. 41, no. 9, pp. 091712-1–091712-13, 2014.
[26] L. Vincent and P. Soille, "Watersheds in digital spaces: An efficient algorithm based on immersion simulation," *IEEE Trans. Pattern Anal. Mach. Intell.*, vol. 13, no. 6, pp. 583–598, Jun. 1991.
[27] V. Grau *et al.*, "Improved watershed transform for medical image segmentation using prior information," *IEEE Trans. Med. Imag.*, vol. 23, no. 4, pp. 447–458, Apr. 2004.
[28] S. Osher and N. Paragios, *Geometric Level Set Methods in Imaging Vision and Graphics*. New York, NY, USA: Springer, 2003.
[29] A. Tsai *et al.*, "A shape-based approach to the segmentation of medical imagery using level sets," *IEEE Trans. Med. Imag.*, vol. 22, no. 2, pp. 137–154, Feb. 2003.
[30] A. K. Robertson *et al.*, "CT, MR, and ultrasound image artifacts from prostate brachytherapy seed implants: The impact of seed size," *Med. Phys.*, vol. 39, no. 4, pp. 2061–2068, 2012.

[31] W. Qiu *et al.*, “Needle segmentation using 3d hough transform in 3d trus guided prostate transperineal therapy,” *Med. Phys.*, vol. 40, no. 4, pp. 042902-1–042902-13, 2013.
[32] D. Borrmann *et al.*, “The 3d hough transform forplane detection in point clouds: A review and a new accumulator design,” *J. 3D Res.*, vol. 2, no. 2 (3 pages), 2011.
[33] F. Zana and J. C. Klein, “A multimodal registration algorithm of eye fundus images using vessels detection and hough transform,” *IEEE Trans. Med. Imag.*, vol. 18, no. 5, pp. 419–428, May 1999.
[34] M. Lahanas *et al.*, “Optimized bounding boxes for three-dimensional treatment planning in brachytherapy,” *Med. Phys.*, vol. 27, pp. 2333–2342, 2000.
[35] J. O’Rourke, “Finding minimal enclosing boxes,” *J. Comput. Inf. Sci.*, vol. 14, pp. 183–199, 1985.
[36] P. Hoskin and C. Coyle, “Radiotherapy in practice-brachytherapy,” in *Radiotherapy in Practice*. Oxford, U.K.: Oxford Univ. Press, 2011.
[37] IsoSeedI-125 (I25.S06) Instructions for Use, BEBIG Company, Berlin, Germany, 2002.
[38] C. Fouard *et al.*, “CamiTK: A modular framework integrating visualization, image processing and biomechanical modeling,” in *Soft Tissue Biomechanical Modeling for Computer Assisted Surgery*. New York, NY, USA: Springer, 2012, pp. 323–354.
[39] F. Meneu *et al.*, “Consideration of seeds orientation in prostate brachytherapy and dosimetric analysis,” *Physica Medica*, vol. 29, pp. e33–e34, 2013.
[40] M. Moradi *et al.*, “Needle path detection for brachytherapy dosimetry based on lateral power imaging and template matching,” in *Proc. IEEE Int. Ultrason. Symp.*, 2009, pp. 1–4.
[41] C. Fekete *et al.*, “Quantifying the effect of seed orientation in postplanning dosimetry of low-dose-rate prostate brachytherapy,” *Med. Phys.*, vol. 41, no. 10, pp. 1017704-1–1017704-9, 2014.

Huu-Giao Nguyen received the Bachelor’s degree from the University of Science, Hochiminh City, Vietnam, in 2004 and the Master’s degree from the University of La Rochelle, France, in 2008. He received the Ph.D. degree in signal processing and telecommunications from the Institut Telecom/Telecom Bretagne, Brest, France in 2011. In 2012, he was a Postdoctoral Fellow at MISTIS team, INRIA Rhne-Alpes, France. He is currently a Researcher at GMCAO team, TIMC-IMAG lab in Grenoble, France. His research interests include image processing, machine learning, and statistical methods applied to medical image, low-level image analysis.

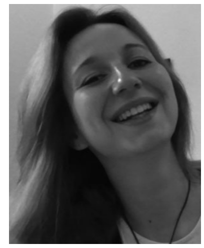

Céline Fouard received the M.S. degree in computer science and image analysis from the University of Bordeaux, Bordeaux, France, in 2001, and the Ph.D. degree in computer science and medical image analysis from the University of Nice Sophia Antipolis, Nice, France, in 2005.

During 2005–2006, she worked on image analysis at the Center for Image Analysis, Uppsala University, Uppsala, Sweden, in the field of discrete geometry. She is currently an Assistant Professor at the Techniques for biomedical engineering and complexity management—informatics, mathematics and applications—Grenoble Laboratory, University of Grenoble, France, where she is involved in teaching computer science and working on computer-assisted medical interventions

Jocelyne Troccaz (SM’15) was born in 1959. She received the Ph.D. degree in computer science from the Institut National Polytechnique de Grenoble, Grenoble Cedex, France, in 1986.

Since 1998, she has been the CNRS Research Director. Until 1990, her activity was in the field of automatic robot programming for industrial and spatial robotics. She moved to Medical Robotics in 1990. Her personal research activity in the TIMC-IMAG laboratory of Grenoble is mainly about the medical applications of robotics and medical image processing. She is involved in several clinical collaborations. She has more than 200 publications including international patents. She has been an Invited Speaker in several conferences. She is on the organising committees of a number of international conferences. She is or has been an Associate Editor for the *Journal of Computer-Aided Surgery*, for the IEEE TRANSACTIONS ON ROBOTICS and for the *International Journal of Medical Robotics and Computer Assisted Surgery* and she is on the editorial board of the Medical Image Analysis Journal.

Dr. Troccaz was elected MICCAI Fellow in 2012 and received in 2014 the "Prize from the French Academy of Surgery" she now belongs to.